



# Interfacial conditions between a free-fluid region and a porous medium

Sahrish B. Naqvi\*, Alessandro Bottaro

Università di Genova, Scuola Politecnica, DICCA via Montallegro 1, Genova, 16145, Italy



## ARTICLE INFO

### Article history:

Received 27 July 2020

Revised 21 January 2021

Accepted 28 January 2021

Available online 3 February 2021

### Keywords:

Homogenization

Multiscale analysis

Free-fluid/porous interface

Darcy-Stokes conditions

Hiemenz flow

Backward facing step

## ABSTRACT

Conditions at the dividing surface between a free-fluid and a porous region are of utmost importance when a two-domain approach is used to treat the coupled problem. Conditions arising from homogenization theory are derived here; they are akin to the classical Beavers-Joseph-Saffman conditions, the difference being that the coefficients which appear in the fluid-porous matching relations stem from the solution of microscopic, Stokes-like problems in a cell around the dividing surface with periodic conditions along the interface-parallel directions, and do not need to be fixed ad-hoc. The case of isotropic porous media is considered, and the model coefficients are provided for both two- and three-dimensional grains, for varying porosity. The relations at the interface are then tested for two problems: the stagnation-point flow over a porous bed and the motion past a backward-facing step, with the step region made of a porous material. To verify the accuracy of the conditions, macroscopic solutions are compared to feature-resolving simulations and excellent agreement is demonstrated, even for values of the Reynolds number larger than those for which the theory is formally applicable and for a large value of the porosity which results in significant infiltration of the fluid into the porous medium.

© 2021 Elsevier Ltd. All rights reserved.

## 1. Introduction

The problem of the coupling between the motion in a free-fluid region and that in a neighboring porous domain saturated by a fluid has been largely studied experimentally (Beavers and Joseph, 1967; Gupte and Advani, 1997; Agelinchaab et al., 2006; Arthur et al., 2009; Morad and Khalili, 2009; Terzis et al., 2019), analytically (Richardson, 1971; Saffman, 1971; Jones, 1973; Chandesris and Jamet, 2006; Jamet and Chandesris, 2009; Lacis and Bagheri, 2016), and numerically (Larson and Higdon, 1986; Liu and Prosperetti, 2011; Carraro et al., 2013; Kuwata and Suga, 2016; 2017), most often with a focus on understanding the nature of interface<sup>1</sup> conditions for simple uni-directional shear flows.

The prototypical example is the laminar flow in a channel bounded by a porous layer, whose analysis was initiated with the experiments by Beavers and Joseph (1967); they observed that the viscous shear from the free-fluid region penetrates into the porous medium ultimately altering the velocity distribution of the fluid in

an intermediate layer across the dividing surface. Such a layer has a thickness of the same order of the characteristic microscale of the porous matrix, typically the interpore distance. Reducing such a layer to a two-dimensional surface (which, for simplicity can be taken to coincide with the dividing fluid-porous surface) permits to express the interface boundary condition as a *slip velocity*, i.e.

$$\hat{u} = \langle \hat{u}^- \rangle + \frac{\hat{\kappa}^{1/2}}{\alpha_{BJ}} \frac{\partial \hat{u}}{\partial \hat{y}}, \quad (1)$$

and analogously for  $\hat{w}$ . The velocity components  $\hat{u}$  and  $\hat{w}$  are parallel to the dividing surface, of normal coordinate  $\hat{y}$  (cf. Fig. 1);  $\alpha_{BJ}$  is an empirical, order one dimensionless constant introduced by Beavers and Joseph;  $\hat{\kappa}$  is the permeability of the porous matrix (a scalar quantity for an isotropic arrangement of pores and solid inclusions). The term  $\langle \hat{u}^- \rangle$  represents the seepage velocity through the porous medium, the superscript  $-$  indicating that the variable is evaluated sufficiently below the dividing line/surface, with angle brackets denoting volume averaging (see later Eq. (37)). Darcy's law stipulates that the mean velocity in the porous medium, away from boundaries, is linearly dependent on the pore pressure gradient, i.e.

$$\langle \hat{u}^- \rangle = -\frac{\hat{\kappa}}{\mu} \frac{\partial \hat{p}^-}{\partial \hat{x}}, \quad (2)$$

\* Corresponding author.

E-mail address: [naqvi.sehrish@yahoo.com](mailto:naqvi.sehrish@yahoo.com) (S.B. Naqvi).

<sup>1</sup> The word "interface" is used interchangeably with the words "dividing line" and "dividing surface" to mean that line or surface which separates the free-fluid region, where the Navier-Stokes equation holds, from the region which can be described by macroscopic equations, such as Darcy's or Brinkman's models.

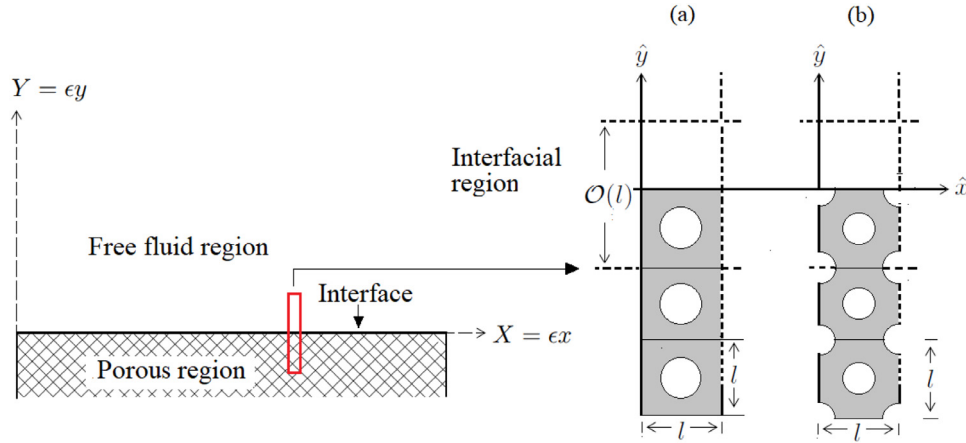


**Fig. 1.** Two-dimensional macroscopic domain together with microscopic cell (shown by red lines). The latter is shown in its dimensional settings on the right: (a) in-line arrangement of solid grains, (b) staggered arrangement.

and similarly for the other two components, with  $\mu$  the dynamic viscosity of the fluid and  $\hat{p}^-$  the interstitial pressure.

Saffman (1971) was the first to provide a theoretical justification for the empirical condition by Beavers and Joseph; he considered the Stokes equations in a domain across the dividing surface and performed asymptotic matching at the two edges of the interface layer. A few other studies along similar lines were conducted after Saffman, leading to similar conclusions (Jäger and Mikelić, 2001; Laciš and Bagheri, 2016). The result by Saffman, when expressed up to second order in terms of the small expansion parameter  $\epsilon$ , ratio of micro- to macro-scale of the problem, takes the form:

$$\hat{u} = -\frac{B\hat{\mathcal{K}}}{\mu} \frac{\partial \hat{p}^-}{\partial \hat{x}} + \hat{\lambda} \frac{\partial \hat{u}}{\partial \hat{y}}, \quad (3)$$

with  $B$  a order one constant used to adapt the permeability of the porous medium to the geometric interface conditions, and  $\hat{\lambda}$  (equal to  $\hat{\mathcal{K}}^{1/2}/\alpha_{Bj}$  in Beavers and Joseph's notations) a slip coefficient. In the equation above the dimensional quantity  $\hat{\mathcal{K}}$ , homogeneous to a surface area, is of order  $\epsilon^2$  and the quantity  $\hat{\lambda}$ , a length, is of order  $\epsilon$ . This prompted Saffman to discard the term containing the pore pressure gradient, and to write the slip velocity at the porous/free-fluid interface in the form of simple Navier slip (for a thorough discussion of Navier slip the reader is referred to Bottaro (2019)).

Conditions such as those proposed by Beavers and Joseph are necessary when the so-called *two-domain* approach is employed, i.e. when the free-fluid region is approached by solving the Stokes or Navier-Stokes equations, and the porous domain is treated by the use of the Darcy (or more elaborate) macroscopic model. Alternatives to the Beavers and Joseph condition have been proposed, e.g., in refs. (Ochoa-Tapia et al., 2017) and (Ochoa-Tapia and Whitaker, 1995).

Instead of the two-domain approach one can also carry out the solution of the volume-averaged Navier-Stokes equations (Whitaker, 1986) across the whole domain. This latter *one-domain* approach has been used successfully by a number of researchers to treat the interface region (Luminari et al., 2019; Angot et al., 1999; Carbou, 2008; Bruneau et al., 2020).

The analysis to follow, for the case of isotropic solid grains, relies on separation of scales; this means that the inter-grain distance must be much smaller than a characteristic length scale of the macroscopic flow in the free-fluid region. We thus divide the whole domain into three portions: an outer free-fluid part (denoted with superscript  $+$ ), an intermediate, thin interfacial region, and a third part (superscript  $-$ ) where the fluid motion is ruled by Darcy's equation. The asymptotic analysis is described in the

next section, and the conditions which hold at a porous-fluid interface, whose position must be set, are derived. All the coefficients pertaining to these conditions are computed and reported in tabular form in Appendix B, for future possible use. In section 3 they are employed to study the macroscopic flow in two different two-dimensional configurations including, in particular, the case of fluid infiltrating a porous domain. These cases, compared against fully feature-resolving simulations, demonstrate the accuracy of the approach even for situations beyond the formal domain of validity of the conditions, including the case of very large porosity parameter or large Reynolds numbers. Concluding remarks are given in section 4.

## 2. Mathematical formulation

A regularly microstructured porous medium is taken to bound a free-fluid region; for reasons of clarity we limit the present analysis to two-dimensional Cartesian coordinates. The porous medium has a characteristic microscopic length scale equal to  $l$  (say, the periodicity of the pattern); the macroscopic length scale is  $L$  (for example, the channel half-thickness). With reference to Fig. 1, the interface where outer flow conditions will be enforced is arbitrarily positioned in  $\hat{y}=0$ , with hat variables denoting dimensional quantities. Other choices are possible for the position, close to  $\hat{y}=0$ , where interface conditions can be enforced, but the results are very weakly dependent on the choice made (for a discussion on this issue, see (Laciš and Bagheri, 2016; Laciš et al., 2020)). The presence of two characteristic scales renders the problem amenable to a multiple scale expansion, in terms of the small parameter  $\epsilon = l/L$ , along the lines of Mei and Vernescu (2009).

### 2.1. Scalings and equations in the three regions

Three regions can be identified, and will be normalized successively, starting from the outer one ( $+$ , or free-fluid region) up to the inner one ( $-$ , or porous region).

In the free-fluid, we use  $L, L/\mathcal{U}, \mathcal{U}$ , and  $\rho\mathcal{U}^2$  to scale, respectively, length, time, velocity and pressure. The velocity  $\mathcal{U}$  is a characteristic speed, for example, the free stream velocity in a boundary layer, and  $\rho$  is the fluid density. The dimensionless system in the  $+$  region is simply

$$\frac{\partial U_i^+}{\partial X_i} = 0, \quad \frac{\partial U_i^+}{\partial t} + U_j^+ \frac{\partial U_i^+}{\partial X_j} = -\frac{\partial P^+}{\partial X_i} + \frac{1}{Re} \frac{\partial^2 U_i^+}{\partial X_j^2}. \quad (4)$$

We define  $X_1 = X = \hat{x}/L$ ,  $X_2 = Y = \hat{y}/L$ ,  $U_1^+ = U^+ = \hat{u}/\mathcal{U}$ , and  $U_2^+ = V^+ = \hat{v}/\mathcal{U}$ ; the macroscopic Reynolds number is  $Re = \rho\mathcal{U}L/\mu$ . No-

tice that all dependent variables in this upper region depend only upon the macroscale spatial coordinates.

The intermediate region, across the dividing line/surface, is denoted by the superscript = ; here we choose  $l = \epsilon L, L/\mu, \epsilon U$ , and  $\mu U/L$  to normalize, respectively, length, time, velocity and pressure. These are the same scales used in countless papers to model the flow over a rough wall, cf. Bottaro and Naqvi (2020) and references therein. The dimensionless equations in the  $y$ -elongated microscopic cell which traverses  $y = 0$  are

$$\frac{\partial U_i^=}{\partial x_i} = 0, \quad \epsilon^2 Re \left( \frac{\partial U_i^=}{\partial t} + U_j^= \frac{\partial U_i^=}{\partial x_j} \right) = -\frac{\partial P^=}{\partial x_i} + \frac{\partial^2 U_i^=}{\partial x_j^2}, \quad (5)$$

with  $x_1 = x = \hat{x}/l$ ,  $x_2 = y = \hat{y}/l$ ,  $U_1^= = U^= = \epsilon^{-1} \hat{u}/\mu$ , and  $U_2^= = V^= = \epsilon^{-1} \hat{v}/\mu$ . All dependent variables are assumed to be periodic along  $x$  (and along  $z$  when in three-dimensions); around the dividing line/surface they are function of both microscale and macroscale coordinates and the latter dependence is immediately apparent upon matching velocity and traction vectors at the upper boundary of the = region, i.e.

$$\lim_{y \rightarrow +\infty} (U^=, V^=) = \frac{1}{\epsilon} \lim_{Y \rightarrow 0^+} (U^+, V^+) \quad (6)$$

and

$$\begin{aligned} \lim_{y \rightarrow +\infty} \left( \frac{\partial U^=}{\partial y} + \frac{\partial V^=}{\partial x}, -P^= + 2 \frac{\partial V^=}{\partial y} \right) \\ = \lim_{Y \rightarrow 0^+} \left( \frac{\partial U^+}{\partial Y} + \frac{\partial V^+}{\partial X}, -Re P^+ + 2 \frac{\partial V^+}{\partial Y} \right). \end{aligned} \quad (7)$$

The flow in the lower ( - ) inter-pore space, sufficiently below the dividing line/surface, is assumed steady and the equations are rendered dimensionless by the same scales as in the interface region, except for replacing  $\epsilon \mu$  by  $\epsilon^2 \mu$  when normalizing the velocity. This choice of scales stems from assuming that the macroscopic pressure gradient is balanced by viscous dissipation within the pores (Mei and Vernescu, 2009). Eventually, in a square unit cell within the porous medium and away from boundaries we should solve

$$\epsilon \frac{\partial U_i^-}{\partial x_i} = 0, \quad \epsilon^4 Re U_j^- \frac{\partial U_i^-}{\partial x_j} = -\frac{\partial P^-}{\partial x_i} + \epsilon \frac{\partial^2 U_i^-}{\partial x_j^2}, \quad (8)$$

subject to periodicity along all spatial directions. This latter system leads to Darcy's equation, after the variables are expanded in power series of  $\epsilon$ , and the leading order terms are retained. The procedure is described in details by Mei and Vernescu (2009); we will not carry it out here, but will develop a composite system valid across the dividing line/surface and below.

## 2.2. The composite description

Here we couple the three regions identified above. Assuming that  $\epsilon^2 Re \ll 1$ , the leading order system in the intermediate domain turns out to be simply Stokes' system. This stems from expanding the generic = variable as

$$F^= (x_i, X_i, t) = F_0^= + \epsilon F_1^= + \epsilon^2 F_2^= + \dots \quad (9)$$

and plugging the expansion into system (5). Since each dependent variable is function of both microscopic and macroscale coordinates, it is important also to replace

$$\frac{\partial}{\partial x_j} \rightarrow \frac{\partial}{\partial x_j} + \epsilon \frac{\partial}{\partial X_j}, \quad (10)$$

to obtain

$$\mathcal{O}(\epsilon^0) : \quad \frac{\partial U_{0i}^=}{\partial x_i} = 0, \quad -\frac{\partial P_0^=}{\partial x_i} + \frac{\partial^2 U_{0i}^=}{\partial x_j^2} = 0, \quad (11)$$

$$\mathcal{O}(\epsilon^1) : \quad \frac{\partial U_{1i}^=}{\partial x_i} = -\frac{\partial U_{0i}^=}{\partial X_i}, \quad -\frac{\partial P_1^=}{\partial x_i} + \frac{\partial^2 U_{1i}^=}{\partial x_j^2} = \frac{\partial P_0^=}{\partial X_i} - 2 \frac{\partial^2 U_{0i}^=}{\partial x_j \partial X_j}. \quad (12)$$

In the - region each generic  $F^-$  variable is expanded as

$$F^- (x_i, X_i) = F_0^- + \epsilon F_1^- + \epsilon^2 F_2^- + \dots \quad (13)$$

and the expansions are plugged into system (8), to obtain

$$\mathcal{O}(\epsilon^0) : \quad \frac{\partial P_0^-}{\partial x_i} = 0, \quad (14)$$

$$\mathcal{O}(\epsilon^1) : \quad \frac{\partial U_{0i}^-}{\partial x_i} = 0, \quad -\frac{\partial P_1^-}{\partial x_i} + \frac{\partial^2 U_{0i}^-}{\partial x_j^2} = \frac{\partial P_0^-}{\partial X_i}, \quad (15)$$

$$\mathcal{O}(\epsilon^2) : \quad \frac{\partial U_{1i}^-}{\partial x_i} = -\frac{\partial U_{0i}^-}{\partial X_i}, \quad -\frac{\partial P_2^-}{\partial x_i} + \frac{\partial^2 U_{1i}^-}{\partial x_j^2} = \frac{\partial P_1^-}{\partial X_i} - 2 \frac{\partial^2 U_{0i}^-}{\partial x_j \partial X_j}. \quad (16)$$

It is a well-established fact that the pressure at leading order in the porous matrix,  $P_0^-$ , does not fluctuate on the pore scale (cf. Eq. (14)).

We now define the composite velocity and pressure fields

$$u_i = u_i^{(0)} + \epsilon u_i^{(1)} + \mathcal{O}(\epsilon^2), \quad (17)$$

$$p = p^{(0)} + \epsilon p^{(1)} + \mathcal{O}(\epsilon^2), \quad (18)$$

with

$$u_i^{(0)} = \begin{cases} U_{0i}^= & y > 0, \\ \epsilon U_{0i}^- & y < 0, \end{cases} \quad (19)$$

$$p^{(0)} = \begin{cases} P_0^= & y > 0, \\ P_0^- + \epsilon P_1^- & y < 0, \end{cases} \quad (20)$$

and

$$u_i^{(1)} = \begin{cases} U_{1i}^= & y > 0, \\ \epsilon U_{1i}^- & y < 0, \end{cases} \quad (21)$$

$$p^{(1)} = \begin{cases} P_1^= & y > 0, \\ \epsilon P_2^- & y < 0. \end{cases} \quad (22)$$

The Ansatz above implies that an abrupt transition is assumed between the = and - regions; this corresponds to what is referred to in the literature as the *two-domain approach*, leading to a jump in pressure across  $y = 0$ . The leading-order composite equations, valid in a neighborhood of  $y = 0$  as well as throughout the porous medium, are

$$\frac{\partial u_i^{(0)}}{\partial x_i} = 0, \quad -\frac{\partial p^{(0)}}{\partial x_i} + \frac{\partial^2 u_i^{(0)}}{\partial x_j^2} = 0, \quad (23)$$

and at next order we have

$$\frac{\partial u_i^{(1)}}{\partial x_i} = -\frac{\partial u_i^{(0)}}{\partial X_i}, \quad -\frac{\partial p^{(1)}}{\partial x_i} + \frac{\partial^2 u_i^{(1)}}{\partial x_j^2} = \frac{\partial p^{(0)}}{\partial X_i} - 2 \frac{\partial^2 u_i^{(0)}}{\partial x_j \partial X_j}. \quad (24)$$

The situation is schematized in Fig. 2.

For  $y \rightarrow -\infty$  (i.e. sufficiently deep inside the porous medium) the solution of system (8) in a  $1 \times 1$  periodic unit cell, eventually leading to the medium permeability, should be recovered. On the top boundary of the interface cell the matching outer-flow conditions (6) and (7) are

$$\lim_{y \rightarrow +\infty} (u, v) = \frac{1}{\epsilon} \lim_{Y \rightarrow 0^+} (U, V), \quad (25)$$

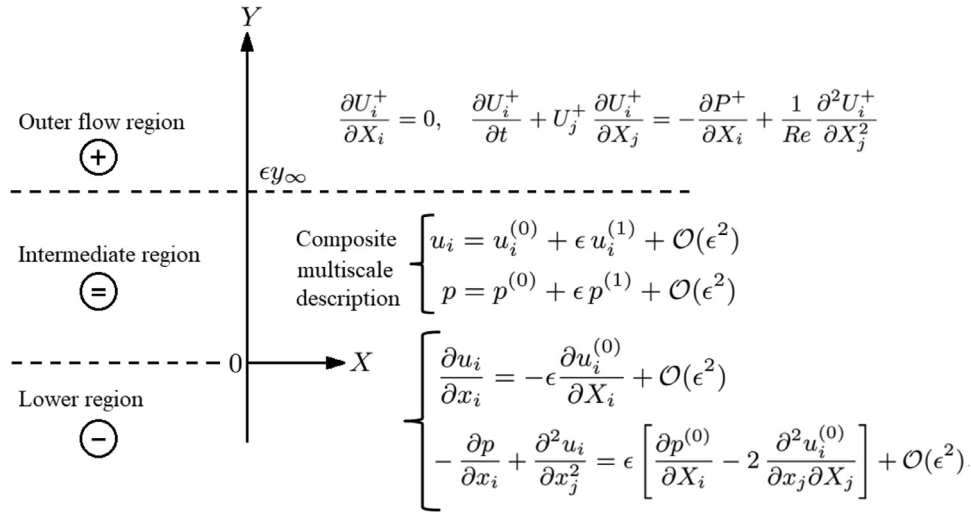


**Fig. 2.** Schematic of the mathematical description of the interface problem, together with equations in the free-flow (+) region and composite, multiscale equations which apply in the = and - regions. In the numerical application, the matching between the flow in the region described by the composite equations and that in the free-fluid region is done at a finite value of  $y$ , i.e.  $y = y_\infty$ .

$$\lim_{y \rightarrow +\infty} \left( \frac{\partial u}{\partial y} + \frac{\partial v}{\partial x}, -p + 2 \frac{\partial v}{\partial y} \right) = \lim_{Y \rightarrow 0^+} \left( \frac{\partial U}{\partial Y} + \frac{\partial V}{\partial X}, -Re P + 2 \frac{\partial V}{\partial Y} \right). \tag{26}$$

Note that from now on we omit the + superscript when referring to dependent variables in the free-fluid region. Also, to simplify notations, we will indicate with  $S^T$  and  $S^N$  the tangential and normal components of the dimensionless macroscopic stress for  $Y \rightarrow 0^+$ , i.e.

$$S^T = \frac{\partial U}{\partial Y} + \frac{\partial V}{\partial X} \Big|_{Y \rightarrow 0^+}, \quad S^N = -Re P + 2 \frac{\partial V}{\partial Y} \Big|_{Y \rightarrow 0^+}. \tag{27}$$

The boundary conditions for (23) at  $y \rightarrow \infty$  become

$$\frac{\partial u^{(0)}}{\partial y} \Big|_{y \rightarrow +\infty} = S^T, \quad -p^{(0)} \Big|_{y \rightarrow +\infty} = S^N, \tag{28}$$

on account of the fact that on the top boundary of the interface cell, by construction,  $u^{(0)} = u_1^{(0)}$ ,  $v^{(0)} = u_2^{(0)}$ , and  $p^{(0)}$  loose memory of the porous matrix microstructure to become independent of  $x$ . The corresponding conditions for the variables at order  $\epsilon$  are:

$$\frac{\partial u^{(1)}}{\partial y} \Big|_{y \rightarrow +\infty} = -\frac{\partial u^{(0)}}{\partial Y} \Big|_{y \rightarrow +\infty} - \frac{\partial v^{(0)}}{\partial X} \Big|_{y \rightarrow +\infty}, \tag{29}$$

$$-p^{(1)} \Big|_{y \rightarrow +\infty} + 2 \frac{\partial v^{(1)}}{\partial y} \Big|_{y \rightarrow +\infty} = -2 \frac{\partial v^{(0)}}{\partial Y} \Big|_{y \rightarrow +\infty}. \tag{30}$$

**2.2.1. Sample solutions of the leading order composite system**

Linearity of system (23) permits to express the velocity components and the pressure using separation of variables, i.e.

$$u_i^{(0)} = u_i^\dagger S^T + u_i^\ddagger S^N, \tag{31}$$

and

$$p^{(0)} = p^\dagger S^T + p^\ddagger S^N + C(X_j). \tag{32}$$

The fields  $u_i^\dagger$ ,  $p^\dagger$ ,  $u_i^\ddagger$ , and  $p^\ddagger$  depend only on  $x_j$ ; conversely, the integration constant  $C$  is only a function of macroscopic coordinates. Plugging (31)–(32) into (23) and (28) permits to find the two systems below, subject to periodicity along  $x$  (and eventually  $z$ , in three-dimensional settings) and to the no-slip condition on the solid grains of the porous medium.

**Forcing by  $S^T$ :**

$$\frac{\partial u_i^\dagger}{\partial x_i} = 0, \quad -\frac{\partial p^\dagger}{\partial x_i} + \frac{\partial^2 u_i^\dagger}{\partial x_j^2} = 0, \tag{33}$$

$$\lim_{y \rightarrow +\infty} \frac{\partial u^\dagger}{\partial y} = 1, \quad \lim_{y \rightarrow +\infty} p^\dagger = 0. \tag{34}$$

**Forcing by  $S^N$ :**

$$\frac{\partial u_i^\ddagger}{\partial x_i} = 0, \quad -\frac{\partial p^\ddagger}{\partial x_i} + \frac{\partial^2 u_i^\ddagger}{\partial x_j^2} = 0, \tag{35}$$

$$\lim_{y \rightarrow +\infty} \frac{\partial u^\ddagger}{\partial y} = 0, \quad \lim_{y \rightarrow +\infty} p^\ddagger = -1. \tag{36}$$

This latter system admits the trivial solution  $u_i^\ddagger = 0$  and  $p^\ddagger = -1$ .

Solutions of the  $\bullet^\dagger$  problem are pursued for both two- and three-dimensional porous media, with either circular or spherical grains, for both in-line or regularly staggered solid inclusions, and for varying porosities. The porosity is defined as  $\theta = \mathcal{V}_{fluid} / \mathcal{V}_{total}$ , with  $\mathcal{V}_{fluid}$  the fluid’s volume in a square unit cell (in a two-dimensional case the volume is meant per unit depth) within the porous domain and  $\mathcal{V}_{total}$  the corresponding total (fluid plus solid) volume. By defining the superficial (or phase) average,

$$\langle a \rangle := \frac{1}{\mathcal{V}_{total}} \int_{\mathcal{V}_{fluid}} a \, dV, \tag{37}$$

the porosity is also  $\theta = \langle 1 \rangle$ . The intrinsic average can also be defined as

$$\langle a \rangle^f := \frac{1}{\mathcal{V}_{fluid}} \int_{\mathcal{V}_{fluid}} a \, dV, \tag{38}$$

to be used later on.

Since only the gradient of  $p^\dagger$  appears in Eq. (33), uniqueness of the solution is guaranteed by imposing

$$\langle p^\dagger \rangle_\infty = 0, \tag{39}$$

with the phase average now taken on the top  $1 \times 1$  square (or cubic) cell of the elongated interfacial domain (this is indicated by the subscript  $\infty$ ). This implies that

$$p^{(0)} \Big|_\infty = \langle p^{(0)} \rangle_\infty = -S^N + C, \tag{40}$$

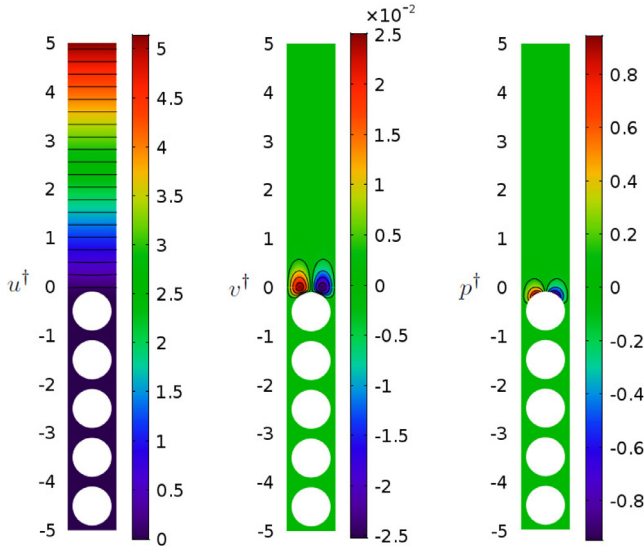


Fig. 3. Fields of  $u^\dagger$ ,  $v^\dagger$  and  $p^\dagger$  for  $\theta = 0.4973$ , regularly arranged two-dimensional solid grains.

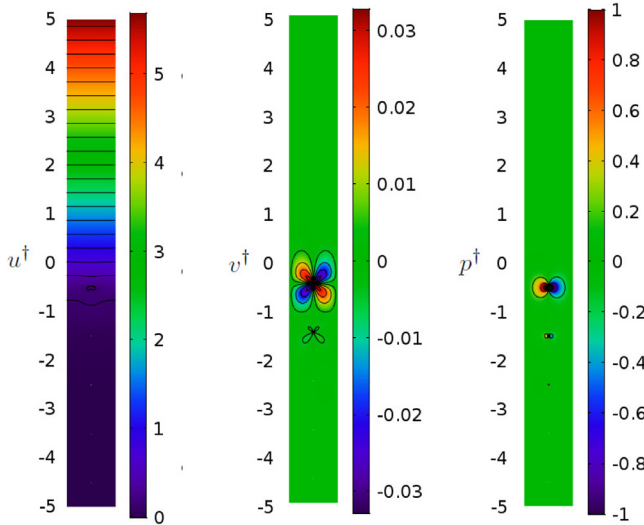


Fig. 4. Same as Fig. 3 for  $\theta = 0.9999$ . The solid inclusions are so small that they are not visible on the scale of the plot.

so that by the second equation in (28) it is finally found

$$C = 0. \quad (41)$$

Solutions of the auxiliary problem (33)–(34) are carried out using the finite elements Comsol Multiphysics® software (COMSOL), progressively refining the mesh until grid-converged solutions are found. Sample results are first provided below, the parametric variation is discussed later. Figs. 3 and 4 display isolines of the unknowns for two values of  $\theta$  in the full domain considered in the two-dimensional in-line case, domain which ranges in  $y$  from  $-y_\infty = -5$  to  $y_\infty = +5$ . Such a vertical extent has been verified against larger values of  $y_\infty$  and it has been found to be sufficient to yield domain-independent results for all porosities tested. In particular,  $y_\infty$  must be sufficiently large for all fields computed to become homogeneous in  $x$  when  $y = +y_\infty$ . The larger value of the porosity considered in Fig. 4 ( $\theta = 0.9999$ ) is not representative of a realistic porous medium, except perhaps for the case of sparse canopies and, as a consequence, it will be shown that slip velocities (at the dividing line/surface) and permeability coefficients are much larger than for lower porosities.

It should also be observed that  $v^\dagger$  and  $p^\dagger$  are antisymmetric around a vertical mid-line (through  $x = 0.5$ ). Thus, for isotropic grains it is  $\int_0^1 v^\dagger dx = 0$  at any  $y$ , and likewise for  $p^\dagger$ .

Just like in the case of the flow over a rough wall (Bottaro and Naqvi, 2020) it is found that

$$u^\dagger|_{y_\infty} = y_\infty + \lambda, \quad (42)$$

with  $\lambda$  a slip length which, for in-line solid inclusions of  $\theta = 0.4973$ , is equal to  $1.451 \times 10^{-1}$ , while  $\lambda = 6.188 \times 10^{-1}$  when the porosity is 0.9999. It is reasonable to expect the slip length (and, as a consequence, the slip velocity) to increase as the solid inclusions become of smaller dimensions. The same values of  $\lambda$  are recovered also by

$$\lambda = \int_0^1 u^\dagger|_{y=0} dx. \quad (43)$$

As in the case of the flow past a rough solid surface (Bottaro and Naqvi, 2020), the outer flow matching

$$u|_{y=y_\infty} = (y_\infty + \lambda) S^T + \mathcal{O}(\epsilon), \quad v|_{y=0^+} = \mathcal{O}(\epsilon). \quad (44)$$

can be transferred to a dividing surface in  $y = 0^+$  and expressed in terms of macroscopic variables (cf. Eq. (25)), for the boundary conditions of the free-fluid variables to read:

$$U|_{y=0^+} = \epsilon \lambda S^T + \mathcal{O}(\epsilon^2), \quad V|_{y=0^+} = \mathcal{O}(\epsilon^2). \quad (45)$$

This is a simple Navier slip condition, aside from the fact that a  $\partial V / \partial X$  term appears in the condition (via  $S^T$ ).

### 2.2.2. The first correction to the leading order composite description

On account of the results obtained for  $u_i^{(0)}$  and  $p^{(0)}$ , system (24) equipped with boundary conditions (29) and (30) becomes

$$\frac{\partial u_i^{(1)}}{\partial x_i} = -u_i^\dagger \frac{\partial S^T}{\partial X_i}, \quad (46)$$

$$-\frac{\partial p^{(1)}}{\partial x_i} + \frac{\partial^2 u_i^{(1)}}{\partial x_j^2} = p^\dagger \frac{\partial S^T}{\partial X_i} - \frac{\partial S^N}{\partial X_i} - 2 \frac{\partial u_i^\dagger}{\partial x_j} \frac{\partial S^T}{\partial X_j}, \quad (47)$$

together with

$$\frac{\partial u_i^{(1)}}{\partial y} \Big|_{y \rightarrow \infty} = -u_i^\dagger \frac{\partial S^T}{\partial Y} - v^\dagger \frac{\partial S^T}{\partial X}, \quad (48)$$

$$-p^{(1)} + 2 \frac{\partial v^{(1)}}{\partial y} \Big|_{y \rightarrow \infty} = -2 v^\dagger \frac{\partial S^T}{\partial Y}. \quad (49)$$

The Ansatz for the new variables is

$$u_i^{(1)} = \tilde{u}_{ij} \frac{\partial S^T}{\partial X_j} + \tilde{u}_{ij} \frac{\partial S^N}{\partial X_j}, \quad (50)$$

$$p^{(1)} = \tilde{p}_j \frac{\partial S^T}{\partial X_j} + \tilde{p}_j \frac{\partial S^N}{\partial X_j}, \quad (51)$$

with the microscopic coefficients arising from the solutions of the two sets of microscopic problems given below.

**Forcing by  $\frac{\partial S^T}{\partial X_j}$ :**

$$\frac{\partial \tilde{u}_{ij}}{\partial x_i} = -u_i^\dagger \delta_{ij}, \quad -\frac{\partial \tilde{p}_j}{\partial x_i} + \frac{\partial^2 \tilde{u}_{ij}}{\partial x_k^2} = p^\dagger \delta_{ij} - 2 \frac{\partial u_i^\dagger}{\partial x_j}, \quad (52)$$

$$\lim_{y \rightarrow +\infty} \frac{\partial \tilde{u}_{1j}}{\partial y} = -u^\dagger \delta_{j2} - v^\dagger \delta_{j1}, \quad \lim_{y \rightarrow +\infty} -\tilde{p}_j + 2 \frac{\partial \tilde{u}_{2j}}{\partial y} = -2 v^\dagger \delta_{j2}. \quad (53)$$

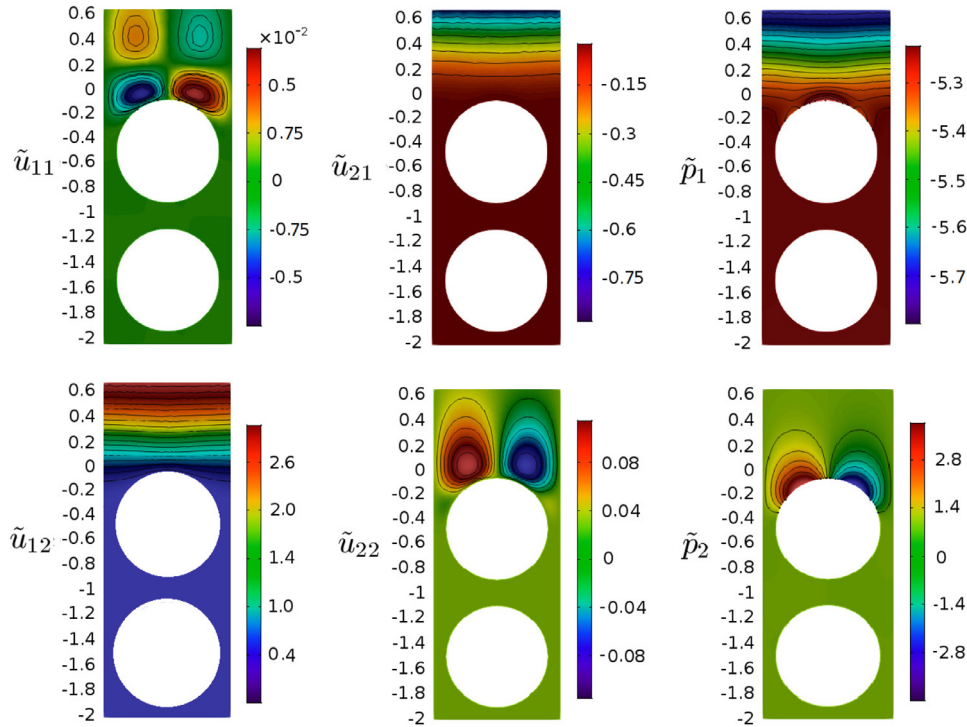


Fig. 5. Fields of  $\tilde{u}_{ij}$  and  $\tilde{p}_j$  in the neighborhood of the dividing surface for regularly arranged two-dimensional solid grains, porosity  $\theta = 0.4973$ .

Forcing by  $\frac{\partial S^N}{\partial X_j}$ :

$$\frac{\partial \tilde{u}_{ij}}{\partial x_i} = 0, \quad -\frac{\partial \tilde{p}_j}{\partial x_i} + \frac{\partial^2 \tilde{u}_{ij}}{\partial x_k^2} = -\delta_{ij}, \quad (54)$$

$$\lim_{y \rightarrow +\infty} \frac{\partial \tilde{u}_{1j}}{\partial y} = 0, \quad \lim_{y \rightarrow +\infty} -\tilde{p}_j + 2 \frac{\partial \tilde{u}_{2j}}{\partial y} = 0. \quad (55)$$

These two systems, like the ones solved earlier, require periodicity along the interface-parallel direction(s); furthermore, the fields deep within the porous domain ( $y \rightarrow -\infty$ ) must repeat themselves with a dimensionless  $y$ -periodicity equal to 1. Numerical solutions of these systems can be easily carried out by the same technique used before; the  $\tilde{\cdot}$  and  $\check{\cdot}$  terms yield all of the  $\mathcal{O}(\epsilon^2)$  terms in the expressions of the macroscopic fields at the interface.

The solution of systems (52)–(53) and (54)–(55) is carried out for varying values of  $y_\infty$ , and results are displayed in Figs. 5 and 6 in the vicinity of the interface, when using  $y_\infty = 5$ . For the system driven by the gradient of  $S^T$  the coefficient of concern here is  $\tilde{u}_{21}$  whereas for that driven by the gradient of  $S^N$  we are interested in  $\tilde{u}_{11}$  and  $\tilde{u}_{22}$ . Other coefficients either vanish at  $y_\infty$  or are antisymmetric about the vertical mid-line so that their  $x$ -averaged value at any  $y$  vanishes. For  $y_\infty$  sufficiently large (larger than about 4), it is found that

$$-\tilde{u}_{21}|_{y_\infty} = \tilde{u}_{11}|_{y_\infty} = \frac{y_\infty^2}{2} + \lambda y_\infty + \mathcal{K}^{itf}, \quad (56)$$

$$\tilde{u}_{22}|_{y_\infty} = \mathcal{K}, \quad (57)$$

with  $\lambda$  the slip length. The other two parameters introduced above are the porous system permeability,  $\mathcal{K}$ , and the interface permeability,  $\mathcal{K}^{itf}$ . For the case reported in Figs. 5 and 6 it is found that  $\mathcal{K} = 1.830 \times 10^{-3}$  and  $\mathcal{K}^{itf} = 1.173 \times 10^{-2}$ .

A result similar to that expressed by (56) was obtained before for the case of the flow past a regularly microstructured, impermeable surface (Bottaro and Naqvi, 2020). We also note that the

same values of the parameters  $\lambda$ ,  $\mathcal{K}$  and  $\mathcal{K}^{itf}$  can be found by the alternative adjoint approach proposed by Bottaro (2019).

If the matching condition (which normally is enforced at  $y_\infty$ ) is conveniently transferred to the dividing surface in  $y = 0^+$ , only  $\mathcal{K}$  and  $\mathcal{K}^{itf}$  enter the interface conditions at second order.

The velocity of the macroscopic problem at  $Y = 0^+$ , correct up to order  $\epsilon^2$  (i.e. including  $u_i^{(0)}$  and  $u_i^{(1)}$ ), has components:

$$U|_{Y=0^+} = \epsilon \lambda S^T|_{Y=0^+} + \epsilon^2 \mathcal{K}^{itf} \frac{\partial S^N}{\partial X}|_{Y=0^+} + \mathcal{O}(\epsilon^3), \quad (58)$$

$$V|_{Y=0^+} = -\epsilon^2 \mathcal{K}^{itf} \frac{\partial S^T}{\partial X}|_{Y=0^+} + \epsilon^2 \mathcal{K} \frac{\partial S^N}{\partial Y}|_{Y=0^+} + \mathcal{O}(\epsilon^3). \quad (59)$$

Eqs. (58) and (59) represent the most important result of the present contribution: the outer flow is coupled to the motion in the porous medium through the coefficients  $\lambda$ ,  $\mathcal{K}$ , and  $\mathcal{K}^{itf}$ , available via the solutions of Stokes-like problems in a  $y$ -elongated cell, periodic along the interface-parallel direction(s). In the expressions above the terms of order  $\epsilon^2$  arise from streamwise and normal variations of the components of the outer traction vector. Eqs. (58) and (59) coincide with those given by Bottaro and Naqvi (2020) for the case of the flow over a rough, impermeable wall, provided the permeability  $\mathcal{K}$  is set to zero; the first term in Eq. (59) is related to transpiration at the surface in  $Y = 0$  because of shear variations.

The condition for  $U|_{Y=0^+}$  does not seem to match (Saffman, 1971)'s, given in dimensional form in (5), since the streamwise velocity at the dividing surface appears to be decoupled from the pore pressure gradient  $\partial P_0^- / \partial Y$  at  $Y = 0^-$ . A further look at the pressure condition is thus needed.

### 2.3. The pressure condition

Continuity of pressure has often been used at the dividing surface (Lacis and Bagheri, 2016; Zampogna et al., 2019); however, the interstitial pressure is a pore-averaged value and, even if the

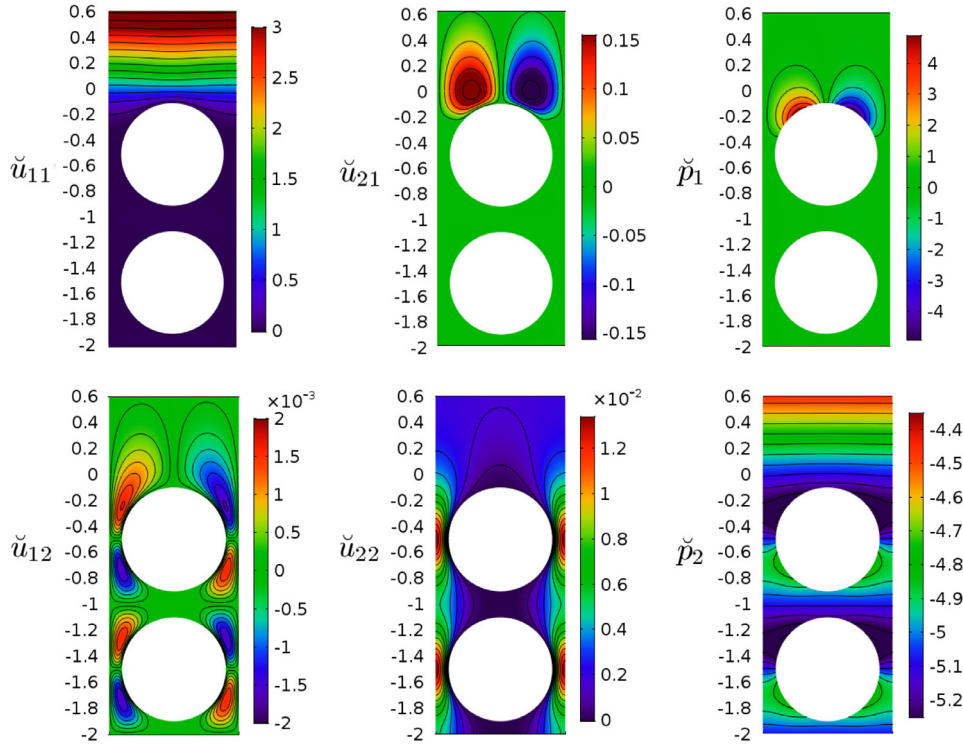


Fig. 6. Same as Fig. 5 for  $\tilde{u}_{ij}$  and  $\tilde{p}_j$ .

microscopic pressure is indeed continuous at  $y = 0$ , it is now accepted that a pressure jump exists between the fluid pressure and the pore pressure, when crossing the interface (Carraro et al., 2013; Lacis et al., 2020). To evaluate such a pressure jump, the starting point is the expression of  $p$  in the interfacial domain, i.e.

$$p = p^\dagger S^T - S^N + \epsilon \tilde{p}_1 \frac{\partial S^T}{\partial X_j} + \epsilon \tilde{p}_2 \frac{\partial S^N}{\partial X_j} + \mathcal{O}(\epsilon^2). \quad (60)$$

Within the porous region the coefficients  $\tilde{p}_1$  and  $\tilde{p}_2$  attain a  $y$ -periodic behavior when we are sufficiently below the dividing surface. The intrinsic average value of the pressure in a  $1 \times 1$  unit cell for  $y \rightarrow -\infty$  is indicated by  $\langle p \rangle_{-\infty}^f$ . We have

$$\langle p \rangle_{-\infty}^f = -S^N + \epsilon \langle \tilde{p}_1 \rangle_{-\infty}^f \frac{\partial S^T}{\partial X} + \epsilon \langle \tilde{p}_2 \rangle_{-\infty}^f \frac{\partial S^N}{\partial Y} + \mathcal{O}(\epsilon^2). \quad (61)$$

Furthermore, from the definition of  $p$  in the porous domain we have

$$\langle p \rangle_{-\infty}^f = P_0^-|_{Y=0^-} + \epsilon \langle P_1^- \rangle_{-\infty}^f + \mathcal{O}(\epsilon^2), \quad (62)$$

so that it is simple to conclude that the normal stress exerted by the outer fluid is impressed onto the pore pressure, i.e.

$$P_0^-|_{Y=0^-} = -S_N + \mathcal{O}(\epsilon). \quad (63)$$

This condition on the leading-order interstitial pressure is sufficient to close the problem and there is no need to find the order one correction to the pressure,  $\langle P_1^- \rangle_{-\infty}^f$ , nor to evaluate the pressure jump across the dividing surface. If the solution in the  $+$  domain is known at iteration  $n$ , boundary condition (63) can be used at the interface for the equation  $\partial^2 P_0^- / \partial X_j^2 = 0$  which describes the behavior of the pore pressure in the bulk of the porous medium. The same condition permits also to write the macroscopic free-fluid streamwise velocity at  $Y = 0^+$  (Eq. (58)) in terms of the pore pressure, i.e. in Saffman's form (cf. Eq. (3)):

$$U|_{Y=0^+} = \epsilon \lambda S^T|_{Y=0^+} - \epsilon^2 \mathcal{K}^{if} \frac{\partial P_0^-}{\partial X} \Big|_{Y=0^-} + \mathcal{O}(\epsilon^3). \quad (64)$$

The vertical velocity at  $Y = 0^+$  can also be expressed in terms of  $P_0^-$  by using Darcy's law, enforcing mass conservation across the interface and accounting for periodicity along the interface-normal boundaries. It reads:

$$V|_{Y=0^+} = -\epsilon^2 \mathcal{K} \frac{\partial P_0^-}{\partial Y} \Big|_{Y=0^-} + \mathcal{O}(\epsilon^3). \quad (65)$$

If (64) and (65) are used at the interface instead of (58) and (59) the motion in the free-fluid region is coupled to that in the porous matrix, i.e. the problems in the two domains must be solved together. Comparison of the two proposed (and equivalent) forms of interface conditions permits to state that also the pressure gradient is discontinuous at the interface; in particular it is easy to find that

$$\text{Re} \frac{\partial P}{\partial X} \Big|_{Y=0^+} - \frac{\partial P_0^-}{\partial X} \Big|_{Y=0^-} = 2 \frac{\partial^2 V}{\partial X \partial Y} \Big|_{Y=0^+} + \mathcal{O}(\epsilon), \quad (66)$$

$$\text{Re} \frac{\partial P}{\partial Y} \Big|_{Y=0^+} - \frac{\partial P_0^-}{\partial Y} \Big|_{Y=0^-} = -\frac{\mathcal{K}^{if}}{\mathcal{K}} \frac{\partial}{\partial X} \left( \frac{\partial U}{\partial Y} + \frac{\partial V}{\partial X} \right) \Big|_{Y=0^+} + 2 \frac{\partial V}{\partial Y} \Big|_{Y=0^+} + \mathcal{O}(\epsilon). \quad (67)$$

Before closing this subsection it is useful to write all the coupling conditions in terms of dimensional variables. The slip and transpiration conditions to be used in the resolution of the outer flow are:

$$\hat{u}|_{0^+} \approx \hat{\lambda} \left( \frac{\partial \hat{u}}{\partial \hat{y}} + \frac{\partial \hat{v}}{\partial \hat{x}} \right) \Big|_{0^+} + \frac{\hat{\mathcal{K}}^{if}}{\mu} \frac{\partial}{\partial \hat{x}} \left( -\hat{p} + 2\mu \frac{\partial \hat{v}}{\partial \hat{y}} \right) \Big|_{0^+}, \quad (68)$$

$$\hat{v}|_{0^+} \approx \frac{\hat{\mathcal{K}}}{\mu} \frac{\partial}{\partial \hat{y}} \left( -\hat{p} + 2\mu \frac{\partial \hat{v}}{\partial \hat{y}} \right) \Big|_{0^+} - \hat{\mathcal{K}}^{if} \frac{\partial}{\partial \hat{x}} \left( \frac{\partial \hat{u}}{\partial \hat{y}} + \frac{\partial \hat{v}}{\partial \hat{x}} \right) \Big|_{0^+}. \quad (69)$$

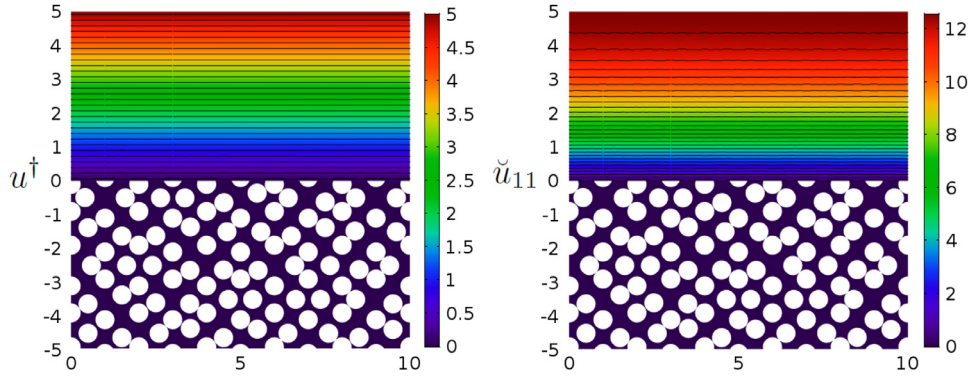


Fig. 7. Fields of  $u^\dagger$  and  $\tilde{u}_{11}$  for  $\theta = 0.4973$ , randomly arranged two-dimensional solid grains.

Alternatively, we can also write

$$\hat{u}|_{0^+} \approx \hat{\lambda} \left( \frac{\partial \hat{u}}{\partial \hat{y}} + \frac{\partial \hat{v}}{\partial \hat{x}} \right) \Big|_{0^+} - \frac{\hat{\kappa}^{if}}{\mu} \frac{\partial \hat{p}}{\partial \hat{x}} \Big|_{0^+}. \quad (70)$$

$$\hat{v}|_{0^+} \approx -\frac{\hat{\kappa}}{\mu} \frac{\partial \hat{p}}{\partial \hat{y}} \Big|_{0^+}. \quad (71)$$

The Dirichlet condition for the pore pressure at the interface is

$$\hat{p}|_{0^-} \approx \hat{p} - 2\mu \frac{\partial \hat{v}}{\partial \hat{y}} \Big|_{0^+}. \quad (72)$$

The dimensional coefficients are  $\hat{\lambda} = \lambda l$ ,  $\hat{\kappa}^{if} = \kappa^{if} l^2$ , and  $\hat{\kappa} = \kappa l^2$ . It is important to stress once more that no empirical coefficients are present in the matching conditions (68)–(72); the coefficients of interest, homogeneous to either a length or an area, are all available through the solution of simple microscopic problems. Such coefficients are discussed in the section 2.5, for both two- and three-dimensional isotropic porous media.

#### 2.4. Randomly arranged grains

Randomly arranged grains, such as those shown in Fig. 7, have also been considered for completeness, by perturbing the position of each grains about its reference value (starting from the staggered configuration). Fig. 7 shows the results obtained in a  $10 \times 10$   $x$ –periodic domain; the left image shows  $u^\dagger$  (which eventually leads to  $\lambda$ ) and the right one shows  $\tilde{u}_{11}$  (which eventually gives

$\kappa^{if}$ ). The values of the permeability of the anisotropic medium is obtained from the method described by Mei and Vernescu (2009), computing all components of the permeability tensor. Once this is done, the two eigenvalues of the tensor are found,  $\kappa_{\max}$  and  $\kappa_{\min}$ , and their geometric average,  $\kappa_{\text{mean}} = \sqrt{\kappa_{\max} \kappa_{\min}}$ , is computed (Airiau and Bottaro, 2020). It is the average value of  $\kappa$  which is reported in Fig. 8 (central frame) with diamond symbols, and compared to the values found for the case of in-line and staggered solid inclusions. It is interesting to observe that the coefficients found,  $\lambda$ ,  $\kappa_{\text{mean}}$  and  $\kappa^{if}$ , are typically included between the staggered and the in-line values, while remaining closer to the former as the porosity varies.

#### 2.5. How do the coupling coefficients change with porosity?

Results for two-dimensional circular and three-dimensional spherical grains are summarized in Figs. 8 and 9, respectively, for both in-line (solid lines) and staggered (dashed) arrangements of the solid inclusions, and for varying values of the porosity. The two-dimensional case of randomly arranged grains is also included in the figure.

In both two-dimensional and three-dimensional configurations the coefficients have a monotonic behavior with  $\theta$ ; both slip length and interface permeability are systematically one order of magnitude larger in the regularly arranged case than in the staggered configuration (at the same value of  $\theta$ ), to be ascribed to the fact that the unit cell right below the interface ( $0 \leq x \leq 1$ ,

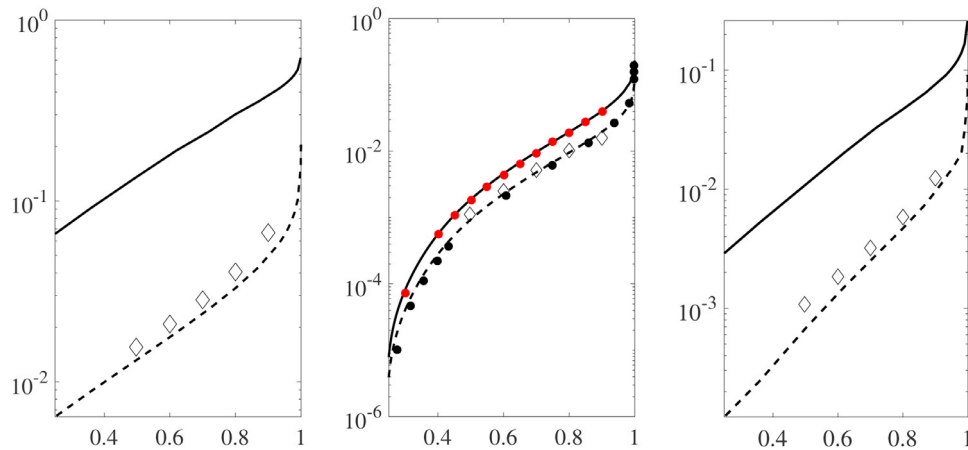
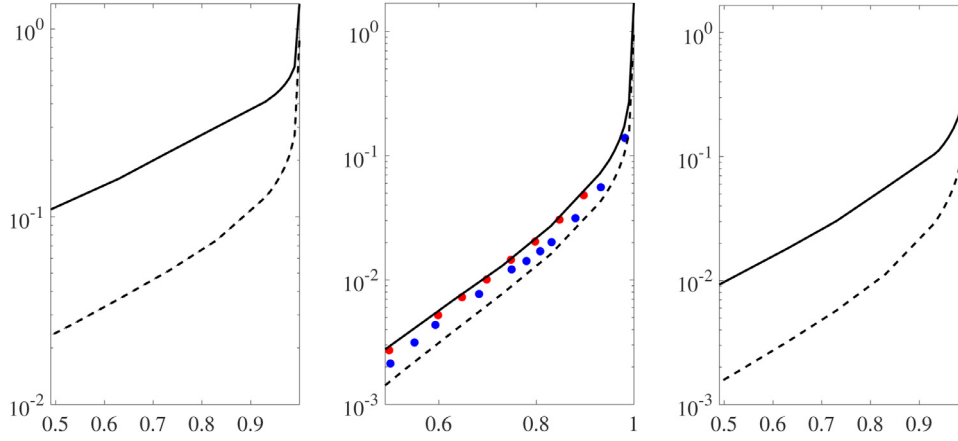


Fig. 8. Comparison between regularly arranged grains (solid lines) and staggered grains (dashed lines) for two-dimensional isotropic porous media of varying porosity  $\theta$  (plotted in abscissa in all frames). From left to right:  $\lambda$ ,  $\kappa$  and  $\kappa^{if}$ . In the central frame the medium permeabilities for in-line and staggered cases are validated, respectively, against (Zampogna and Bottaro, 2016) (red circles) and (Bottaro, 2019) (black circles). The case of randomly arranged grains is also considered (diamond symbols). (For interpretation of the references to color in this figure legend, the reader is referred to the web version of this article.)



**Fig. 9.** Same as Fig. 8 for three-dimensional spherical grains. In the central frame the permeability for the in-line arrangement of spheres is compared to results in (Zampogna and Bottaro, 2016) (red circles). The permeability results for Wigner-Seitz grains (Lee et al., 1996) are given with blue filled symbols. (For interpretation of the references to color in this figure legend, the reader is referred to the web version of this article.)

$-1 \leq y \leq 0$ ) in the staggered case presents a sizeable portion in  $y = 0$  where the fluid cannot slip and through which it cannot penetrate (cf. Fig. 1). Conversely, the deviation in  $\mathcal{K}$  between the two arrangements of solid grains examined is rather small. In the two-dimensional case (Fig. 8) for both grains arrangements the present procedure yields results in excellent agreement with those reported in the past (Zampogna and Bottaro, 2016; Bottaro, 2019), obtained from the conventional approach described by Mei and Vernescu (2009).

For three-dimensional spherical grains, conditions 68–(72) remain unchanged, and must be supplemented by the following spanwise slip condition:

$$\hat{w}|_{0^+} = \hat{\lambda} \left( \frac{\partial \hat{w}}{\partial \hat{y}} + \frac{\partial \hat{v}}{\partial \hat{z}} \right) \Big|_{0^+} - \frac{\hat{\mathcal{K}}^{if}}{\mu} \frac{\partial \hat{p}}{\partial \hat{z}} \Big|_{0^-}, \quad (73)$$

with the same coefficients used in  $\hat{u}$ . The results for  $\mathcal{K}$  in Fig. 9 coincide with those computed by Zampogna and Bottaro (2016), cf. solid line and red dots in the central frame of the figure. It is also instructive to compare the permeability found to that of the Wigner-Seitz grain (Lee et al., 1996), a polyhedron with 14 sides in a cubically packed array, with contact among grains on the six faces of the unit cell. The results of the Wigner-Seitz grain are contained between those of in-line and staggered spherical inclusions, and this denotes the low sensitivity of  $\mathcal{K}$  to the arrangement (and to the exact shape) of the solid grains.

As anticipated in the introduction, all the coefficients computed are tabulated in Appendix A: all the numbers reported are converged up to four significant digits. We have initially tried to find correlations for  $\lambda$ ,  $\mathcal{K}$  and  $\mathcal{K}^{if}$  as function of the porosity  $\theta$  (in a way similar to what done for  $\mathcal{K}$  by Zampogna and Bottaro (2016) for the case of in-line spherical grains) but have eventually decided that it is preferable to give the raw numbers and let eventually interested readers interpolate the tabulated values to infer the coefficients at any desired value of the porosity. This is simpler and more accurate than using a curve-fitting law.

### 3. The macroscopic problems

#### 3.1. Interface conditions

Let us now assume that all dimensional variables, throughout the whole domain, are rendered dimensionless with the same scales used in the free-fluid region. In particular, from now on we denote by  $P_0^-$  the pore pressure non-dimensionalized with  $\rho U^2$ . If the dividing surface is positioned in  $Y = 0$  the conditions to be

imposed there for a two-dimensional macroscopic flow problem, correct up to order 2 in  $\epsilon$ , are:

$$U|_{Y=0^+} \approx \epsilon \lambda \left( \frac{\partial U}{\partial Y} + \frac{\partial V}{\partial X} \right) \Big|_{Y=0^+} + \epsilon^2 \mathcal{K}^{if} \frac{\partial}{\partial X} \left( -Re P + 2 \frac{\partial V}{\partial Y} \right) \Big|_{Y=0^+}, \quad (74)$$

$$V|_{Y=0^+} \approx -\epsilon^2 \mathcal{K}^{if} \frac{\partial}{\partial X} \left( \frac{\partial U}{\partial Y} + \frac{\partial V}{\partial X} \right) \Big|_{Y=0^+} + \epsilon^2 \mathcal{K} \frac{\partial}{\partial Y} \left( -Re P + 2 \frac{\partial V}{\partial Y} \right) \Big|_{Y=0^+}. \quad (75)$$

With the conditions above there is no direct coupling between the Navier-Stokes and the Darcy regions: once the outer flow problem is solved for, the pore pressure at leading order within the isotropic porous medium is a harmonic function which satisfies

$$\frac{\partial P_0^-}{\partial X_i} n_i = 0, \quad (76)$$

at solid surfaces of unit normal  $n_i$ , and

$$P_0^-|_{Y=0^-} = P|_{Y=0^+} - \frac{2}{Re} \frac{\partial V}{\partial Y} \Big|_{Y=0^+} \quad (77)$$

at the dividing surface.

An alternative to conditions (74)–(75), formally correct up to the same order in  $\epsilon$ , is constituted by the following dimensionless conditions:

$$U|_{Y=0^+} \approx \epsilon \lambda \left( \frac{\partial U}{\partial Y} + \frac{\partial V}{\partial X} \right) \Big|_{Y=0^+} - \epsilon^2 \mathcal{K}^{if} Re \frac{\partial P_0^-}{\partial X} \Big|_{Y=0^-}, \quad (78)$$

$$V|_{Y=0^+} \approx -\epsilon^2 \mathcal{K} Re \frac{\partial P_0^-}{\partial Y} \Big|_{Y=0^-}. \quad (79)$$

Conditions (78)–(79) are, respectively, a Beavers-Joseph-like condition for the velocity along the direction tangent to the interface, and an expression of mass conservation across the two domains; they must be coupled to the Laplace equation for the pore pressure in the porous medium, using Eq. (77) which expresses the balance of normal forces at the interface. This latter system is closer to what is often found in the literature (cf. Eggenweiler and Rybak (2020) and references therein). We have employed both sets of conditions to compute the macroscopic results presented below, finding negligible differences.

It is important to notice that Saffman's result, see Eq. (3) in the present paper, is equivalent to (78). In dimensionless form, the result by Saffman, including Jones (1973) correction<sup>2</sup>, reads:

$$U|_{Y=0^+} \approx \epsilon \lambda \left( \frac{\partial U}{\partial Y} + \frac{\partial V}{\partial X} \right) \Big|_{Y=0^+} - \epsilon^2 B \mathcal{K} Re \frac{\partial P_0^-}{\partial X} \Big|_{Y=0^-}. \quad (80)$$

Eqs. (78) and (80) coincide once the constant  $B$  is set equal to  $\mathcal{K}^{itf}/\mathcal{K}$ . The important result of the present contribution is that microscopic problems have been derived and solved for isotropic porous media which yield directly the required constants,  $\lambda$ ,  $\mathcal{K}$ , and  $\mathcal{K}^{itf}$ .

The approach proposed here can be used to solve cases in which the fluid flows parallel to the porous layer or infiltrates the porous medium. Whereas the first case has been much examined in the literature, the latter has been scarcely focussed upon. A recent paper by Eggenweiler and Rybak (2020) shows that the Beavers and Joseph condition is unsuited for filtration problems, and that the parameters of the Beavers-Joseph condition cannot be fitted for arbitrary flow direction. In the following we will examine how the present approach fares when compared to fully resolved simulations which capture microscopic details of flow and pressure fields also within the pores.

### 3.2. Test case 1: stagnation point flow over a porous bed

The first configuration considered is that of the stagnation point flow, with the fluid impacting onto a permeable surface; the porous domain (in  $\hat{y} < 0$ ) is assumed isotropic and the porosity is very large ( $\theta = 0.9999$ ) to allow for large infiltration of the fluid within the porous domain. The small parameter  $\epsilon$  is set to  $\epsilon = 0.1$ , i.e. there are  $10^2$  two-dimensional circular grains in every macroscopic  $1 \times 1$  area.

In the inviscid, irrotational approximation the velocity components in the free fluid are:

$$\hat{u} = a\hat{x}, \quad \hat{v} = -a\hat{y}. \quad (81)$$

The irrotational outer motion is used in the Hiemenz similarity solution far from the (smooth or regularly micro-structured) wall (Bottaro and Naqvi, 2020). In the present configuration a general similarity solution does not exist, because of the Navier-Stokes/Darcy coupling across the interface. In the expressions above, the constant  $a$  is the inverse of a time scale; the characteristic velocity can thus be chosen as  $aL$ . The length scale  $L$  is here the depth of the porous layer; the domain has length  $15L$  along  $\hat{x}$ , and the outer edge is set in  $\hat{y} = 5L$ . Symmetry boundary conditions are employed on the  $\hat{x} = 0$  axis so that the flow develops only in the positive  $\hat{x}$  direction (cf. Fig. 10).

The full Navier-Stokes equations are used in the computations, either resolving the flow field over and within the porous bed, or coupling the solution in  $Y > 0$  to the harmonic pressure field in the porous region, in the manner described before. The same finite elements method is employed for these macroscopic simulations as that used for the microscopic systems in section 2.

We choose a Reynolds number  $Re = aL^2/\nu = 25$ . To account for the presence of a boundary layer, in enforcing the inflow condition the vertical coordinate must be shifted by a quantity equal to the displacement thickness  $\delta_1$ , i.e. at  $Y = 5$ , outer edge of the domain, the inflow conditions in dimensionless form reads:

$$U = X, \quad V = -Y + \delta_1. \quad (82)$$

The dimensionless displacement thickness  $\delta_1$  is *a priori* unknown and it arises as part of the solution. Just like in the case of the

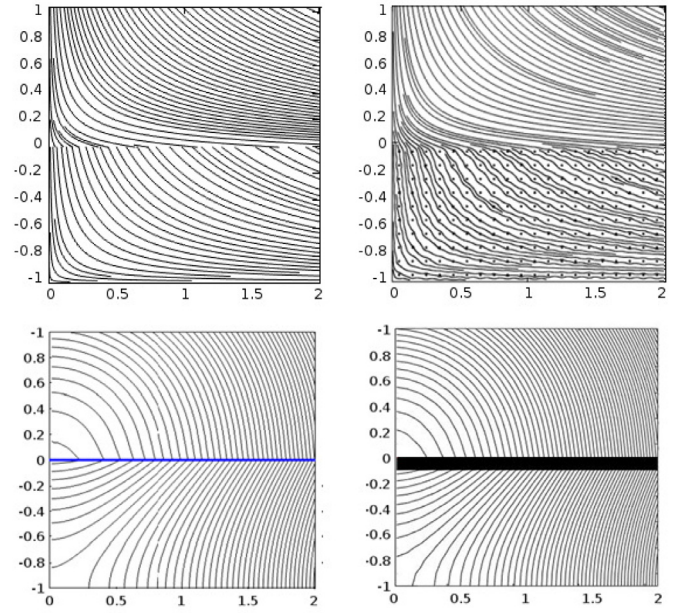


**Fig. 10.** Streamlines (top row) and pressure contours (bottom row) close to the axes' origin, both in the free-fluid and the porous region. The frames on the left correspond to solutions obtained with the two-domain approach; results on the right are obtained by fully resolving the flow, also through the solid inclusions. The pressure in the bottom right frame is the intrinsic averaged pressure.

Hiemenz flow, also here we find that the boundary layer has a constant thickness, i.e.  $\delta_1$  is constant. On the  $X = 15$  boundary the usual *do-nothing* condition is employed when the full Navier-Stokes conditions are employed, and this corresponds to zeroing the traction components. When using the two-domain approach, the condition for  $P_0^-$  in  $Y < 0$  is  $\partial^2 P_0^- / \partial X^2 = 0$  for  $X = 15$ . This amounts to setting to zero the  $Y$ -component of the phase-averaged velocity in the porous medium at the exit plane, an acceptable approximation if the exit boundary is sufficiently far away from the stagnation point.

In the smooth wall case, it is  $\hat{\delta}_1 = 0.648\sqrt{\nu/a}$ , while when the isotropic porous structures are present below the free-fluid region, the displacement thickness decreases to  $0.425\sqrt{\nu/a}$ . The result in the feature-resolving simulation is displayed in Fig. 10 in the vicinity of the point of symmetry ( $X = Y = 0$ ) by the use of streamlines. It is immediately apparent that the fluid both slips at the fictitious wall and traverses it. This is thus a more difficult test case compared to the often used one of the flow is a plane channel bounded by one (or two) porous layers.

In Fig. 11, the solution  $U$  is displayed as a function of  $Y$ , at three different positions,  $X = 1, 2$  and  $3$ , for both direct simulations and for the case in which slip/transpiration conditions are imposed. It is clear that the solution of the feature-resolving simulation, which oscillates along  $Y$  when  $Y < 0$  because of the presence of solid grains, matches well the modeled case.

This result also shows that the velocity component  $U$  in the model problem has a discontinuity close to the interface because of the presence of reasonably large slip speed. The right frame in the Fig. 11 presents the normal velocity component  $V$  as a function of  $Y$  at  $X = 3$  only, since all solutions at different  $X$  positions coincide with one another.

The intrinsic averaged pressure contours in both cases are displayed in Fig. 10 (bottom row). The blue line in the left image corresponds to the dividing surface, across which a pressure jump occurs (cf. Eq. (77)). In the image on the right, the intrinsic average pressure, computed over each unit cell  $\mathcal{V}_f$  of the domain, is displayed for the feature-resolving simulation. The pressure field

<sup>2</sup> Jones replaced the scalar product of the interface-normal unit vector times the free-fluid velocity gradient with the scalar product of the same unit normal vector times the rate of strain tensor.

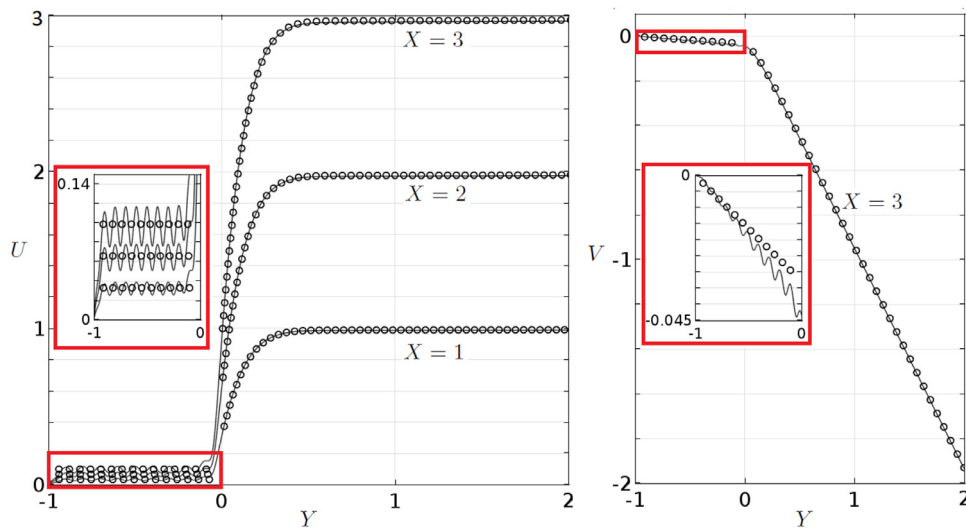


Fig. 11. Comparison between complete simulation with full feature resolution (solid lines) and modeled with slip/transpiration velocity imposed at the dividing line/surface (empty circles). Longitudinal velocity component  $U$  (left) and normal velocity component  $V$  (right) as a function of  $Y$ . The insets highlight the velocity distributions in the porous domain.

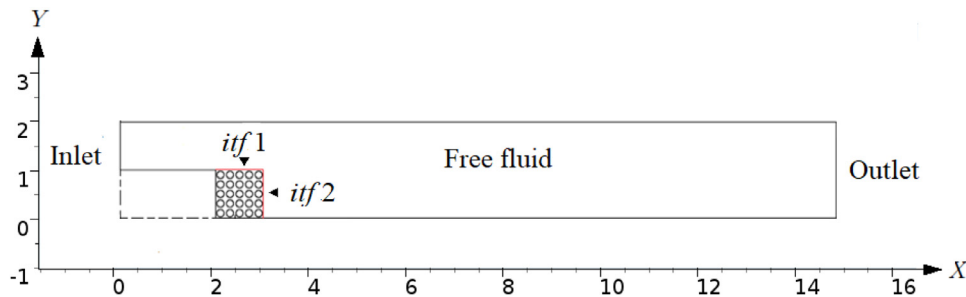


Fig. 12. Computational domain of backward facing step case, with porous block at the step.

and its gradient are discontinuous at  $Y = 0$  also in the right image; the computed pointwise pressure is irregular around the dividing line/surface when the fluid enters the porous region because large local values of the pressure occur near the stagnation points of the uppermost solid grains. There is thus a transition region of dimensional size of order  $l$  (cf. Fig. 10, inset), highlighted with a black strip, across which a jump in intrinsic averaged pressure occurs.

We believe that the results presented in this section represents convincing evidence of the accuracy and applicability of the proposed methodology to treat the dividing surface between a free fluid and a porous region, even when the fluid infiltrates significantly within the porous domain. The results are all the more significant after considering that they have been obtained for an extremely large value of the porosity ( $\theta = 0.9999$ ) and a rather large value of the expansion parameter ( $\epsilon = 0.1$ ). In the next section, another case is considered with two orthogonal intersecting Navier-Stokes/Darcy interfaces, and a value of  $\theta$  smaller than that considered so far. We will also test reasonably large values of the Reynolds number, stretching the limits of applicability of the theory, to assess whether the conditions proposed can be employed for  $Re$  beyond order one.

### 3.3. Test case 2: backward facing step

We now focus on testing the interfacial conditions between the free fluid and the porous domains for the case of the two-dimensional incompressible fluid flow past a backward-facing step,

with the step region made of a isotropic porous material as sketched in Fig. 12.

The porous block occupies the area  $2 \leq X \leq 3$  and  $0 \leq Y \leq 1$ . The domain is long 15 units in  $X$ , and the unit of length corre-

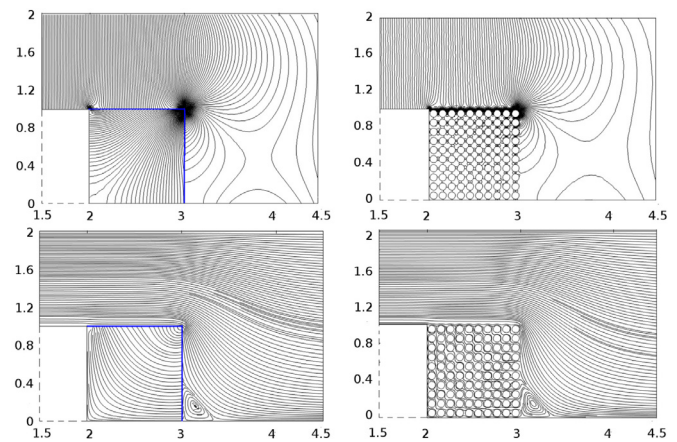


Fig. 13. Comparison between the solutions for  $Re = 0.0001$  of the two-domain approach (left frames, with blue lines denoting the dividing surfaces) and the exact feature-resolving numerical solution of the equations, also through the pores (right frames), focussing around the neighborhood of the step. The top row of images displays the pressure contours; streamlines are plotted in the bottom row.

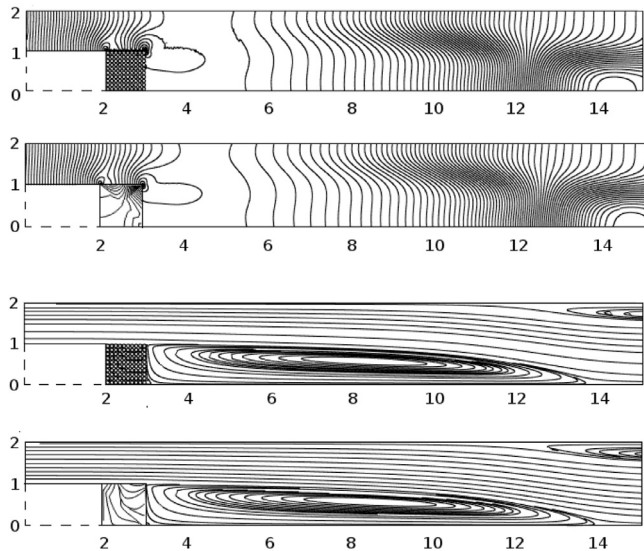


Fig. 14. Same quantities as in Fig. 13, plotted in the whole domain ( $Re = 500$ ).

sponds to either the inflow section or the step height. The horizontal interface,  $itf1$ , is located in  $Y = 1$  and  $2 \leq X \leq 3$ ; the vertical interface,  $itf2$ , is in  $X = 3$  and  $0 \leq Y \leq 1$ . At the inflow of the domain ( $X = 0$ ), the laminar, fully developed channel flow velocity distribution is imposed, i.e.

$$U = 4(Y - 1)(2 - Y) \quad \text{and} \quad V = 0; \quad (83)$$

thus, the centerline velocity at  $X = 0$  and  $Y = 1.5$  is the velocity scale, used in the definition of the Reynolds number  $Re$ . At the outflow ( $X = 15$ ) the traction vector is set to zero. At the solid walls the usual no-slip conditions apply, except on the dividing surfaces,  $itf1$  and  $itf2$ , where we apply the interface conditions derived here.

The case  $\epsilon = 0.1$  and  $\theta = 0.4973$  is considered and the first comparisons, in terms of isobars and streamlines, are made for both a Stokes flow (Fig. 13) and a case with significant inertial effects (Fig. 14).

At this latter value of  $Re$  ( $Re = 500$ ) the flow is still two-dimensional and steady, according to Biswas et al. (2004), when the step is impermeable. The steady solutions we have computed for the permeable step, based on both fully feature-resolving simulations and the two-domain macroscopic approach, attest to the accuracy of the proposed interface conditions: both pressure and streamfunction show the same trends, also for the larger  $Re$  flow. In this latter case the primary recirculation region after the step extends almost up to the domain's exit, and a secondary bubble appears on the upper wall. On the contrary, in the Stokes' flow case the primary recirculating vortex is very small, with both approaches. Although these comparisons seem already to be sufficiently satisfactory, a closer look in the immediate vicinity of  $itf1$  and  $itf2$  is in order

The slip and transpiration velocity components along the two interfaces are plotted in Fig. 15, together with the pressure  $P$ , for the two Reynolds numbers already shown.

The exact feature-resolving results and those obtained by using the interfacial conditions agree well with one another, with the former solutions displaying oscillations on the pore scale, of increasing amplitude with  $Re$ . Such oscillations clearly cannot be captured by the homogenization approach. Notable differences oc-

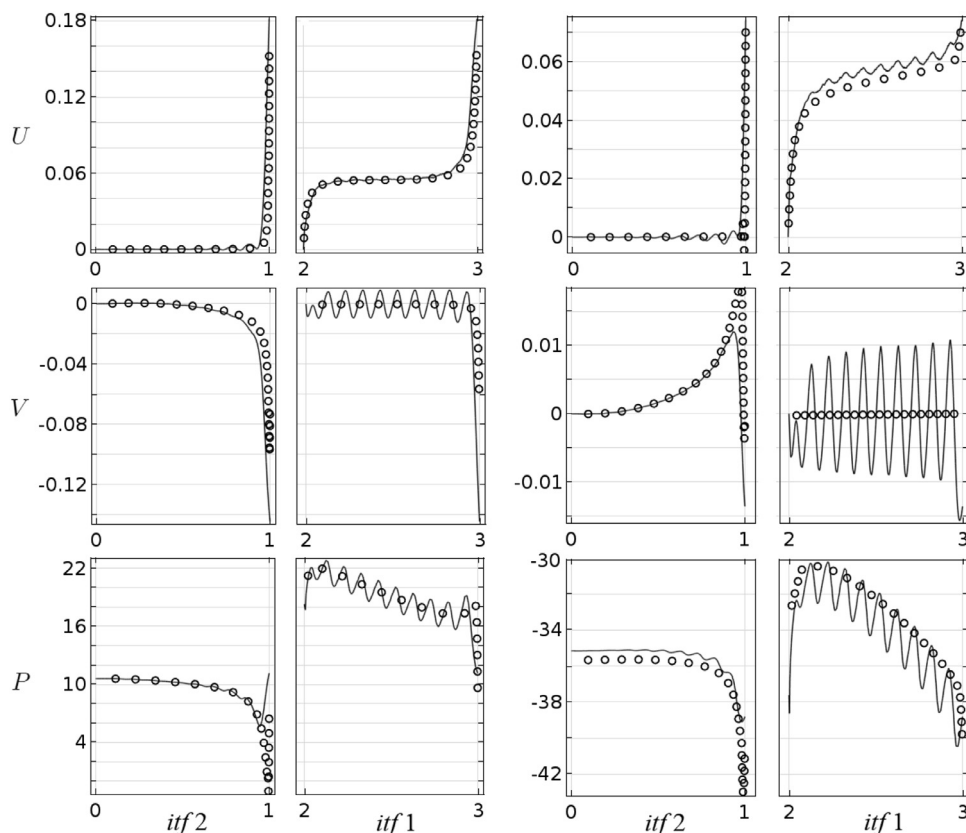
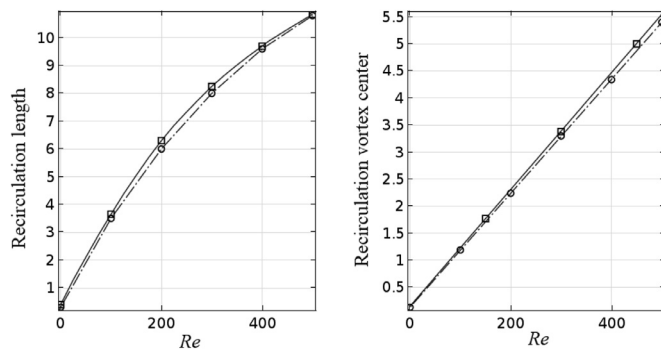


Fig. 15. Comparison of velocity components  $U$ ,  $V$  and pressure  $P$  for  $Re = 0.0001$  (six frames on the left) and  $Re = 500$  (six frames on the right), for the two interfaces. The feature-resolving solutions are shown with solid lines and results of the two-domain approach are displayed with symbols.



**Fig. 16.** Recirculation length and distance of the primary vortex center from the backward-facing step as a function of Reynolds numbers, for the *exact* solutions (dash-dotted lines) and those obtained by using the homogenization approach (circles). Results of simulations without the porous block are shown with solid lines and are compared to reference values by Biswas et al. (2004) (square symbols).

cur, not unexpectedly, at the corner point in  $(X, Y) = (3, 1)$ , where the approximations made break down. The level of accuracy of the model derived here is, however, surprising, particularly for the larger value of the Reynolds number.

A last comparison is made on the primary recirculating vortex after the step, comparing the two approaches in terms of reattachment point and abscissa of the vortex center. Both quantities are measured with respect to the base of the step, in  $X = 3$ . Such comparisons are displayed in Fig. 16. Also on this macroscopic measure the model performs very well, with the results being practically superposed (to graphical accuracy) to those available by carrying out fully resolved numerical simulations. In the figure a further comparison is made for the case  $\theta = 0$ , i.e. when the porous block is impermeable. The results we have obtained match very well those reported by Biswas et al. (2004), obtained for a slightly lower expansion ratio, confirming the validity of our numerical approach.

When the step is porous the recirculation length is slightly shorter (and so is the abscissa of the vortex center) at each Reynolds number. Although the reduction is very small since no attempt has been made to optimize porosity, permeability, or length-scale ratio, this observation provides support on the use of porous panels to mitigate vortex shedding behind bodies.

#### 4. Conclusions

Homogenization theory is a powerful tool to be employed when small-scale features coexist with macroscopic ones. In the present paper we have considered how a idealized porous medium, formed by isotropic (circular or spherical) solid grains of small dimensions, affects the free-fluid flow in its proximity. To achieve our goal, we have divided the whole domain into three regions: an *outer* or *upper* region, where only macroscopic variables are present; an *intermediate* region, across a dividing line/surface, whose dependent variables are function of both micro- and macro-scale variables; a *inner* or *lower* region, deep within the porous medium. The microscopic cell of the intermediate region spans, along the interface-normal direction, from the inner to the outer domain, where the behaviors are either known or can be computed. Such behaviors provide the boundary conditions to be enforced on the dependent

variables of the intermediate reference cell, which has unit length along the interface-parallel, periodic directions. Expanding the unknowns in powers of the small parameter  $\epsilon$ , ratio of microscopic to macroscopic length scales, Stokes-like systems arise at leading order and at next higher order in the intermediate reference cell. These linear systems can be expressed in terms of the forcing terms, related to the traction exerted by the outer flow and its gradient. The auxiliary problems thus arising in the intermediate cell permit to identify three important parameters: a slip length, an interface permeability, and a medium permeability. These are the parameters which represent the effect of the porous domain on the outer, large-scale flow and enter the interface conditions (58) and (59). Of note is the fact that the interface permeability,  $\mathcal{K}^{if}$ , has a different behavior from the porous medium permeability,  $\mathcal{K}$ , particularly at low values of the porosity; this is because a tight packing of the grains affects the flow through the inner region more than it does near the dividing surface. Another important observation concerns the pressure (the outer pointwise value and the inner interstitial value) is not continuous nor differentiable at the interface.

The most significant result of the present paper is represented by the interface conditions, given in dimensional form in Section 2.3, and by the coupling coefficients, Section 2.5. To permit the immediate use and testing of these conditions, for both two- and three-dimensional arrangements of isotropic solid grains, the coefficients are given in Appendix A, as function of the medium porosity.

Our own tests of interface conditions and coefficients have been carried out in a simple two-dimensional setting, under rather straining conditions: significant fluid infiltration through the pores, values of  $\epsilon$  not so small, Reynolds number beyond the Stokes regime. Despite these difficulties the conditions given have performed very well, even beyond expectations, when model computations are compared against simulations which resolve microscopic details also within the porous medium. The cases considered are *i*) the incompressible Hiemenz boundary layer flow over the porous bed and *ii*) the backward facing step, with a porous step region. Additional test cases, possibly including a three-dimensional turbulent flow in the free-fluid region, will be considered in future work.

The extension of the theory to the case of anisotropic porous media does not present fundamental nor numerical difficulties.

#### Declaration of Competing Interest

The authors do not report any conflict of interest.

#### CRediT authorship contribution statement

**Sahrish B. Naqvi:** Formal analysis, Software, Validation, Visualization, Investigation, Writing - review & editing. **Alessandro Bottaro:** Supervision, Conceptualization, Methodology, Investigation, Writing - review & editing, Writing - original draft.

#### Acknowledgements

The financial support of the Italian Ministry of University and Research, program PRIN 2017, project 2017X7Z8S3 LUBRI-SMOOTH, is gratefully acknowledged.

## Appendix A. Coefficients of the interface conditions

Two dimensional case						
$\theta$	In-line			Staggered		
	$\lambda$	$\mathcal{K}$	$\mathcal{K}^{if}$	$\lambda$	$\mathcal{K}$	$\mathcal{K}^{if}$
0.2500	$6.571 \times 10^{-2}$	$8.918 \times 10^{-6}$	$2.896 \times 10^{-3}$	$6.400 \times 10^{-3}$	$3.920 \times 10^{-6}$	$1.223 \times 10^{-4}$
0.3600	$9.147 \times 10^{-2}$	$2.962 \times 10^{-4}$	$5.268 \times 10^{-3}$	$8.872 \times 10^{-3}$	$1.479 \times 10^{-4}$	$2.469 \times 10^{-4}$
0.4973	$1.451 \times 10^{-1}$	$1.830 \times 10^{-3}$	$1.173 \times 10^{-2}$	$1.315 \times 10^{-2}$	$9.100 \times 10^{-4}$	$6.600 \times 10^{-4}$
0.5000	$1.362 \times 10^{-1}$	$1.877 \times 10^{-3}$	$1.089 \times 10^{-2}$	$1.325 \times 10^{-2}$	$9.348 \times 10^{-4}$	$6.775 \times 10^{-4}$
0.6200	$1.899 \times 10^{-1}$	$5.378 \times 10^{-3}$	$2.032 \times 10^{-2}$	$1.871 \times 10^{-2}$	$2.665 \times 10^{-3}$	$1.516 \times 10^{-3}$
0.7200	$2.420 \times 10^{-1}$	$1.120 \times 10^{-2}$	$3.319 \times 10^{-2}$	$2.531 \times 10^{-2}$	$5.518 \times 10^{-3}$	$2.848 \times 10^{-3}$
0.8000	$3.013 \times 10^{-1}$	$1.945 \times 10^{-2}$	$4.691 \times 10^{-2}$	$3.294 \times 10^{-2}$	$9.530 \times 10^{-3}$	$4.694 \times 10^{-3}$
0.8700	$3.542 \times 10^{-1}$	$3.201 \times 10^{-2}$	$6.456 \times 10^{-2}$	$4.293 \times 10^{-2}$	$1.559 \times 10^{-2}$	$7.496 \times 10^{-3}$
0.9300	$4.144 \times 10^{-1}$	$5.798 \times 10^{-2}$	$8.957 \times 10^{-2}$	$5.729 \times 10^{-2}$	$2.547 \times 10^{-2}$	$1.224 \times 10^{-2}$
0.9500	$4.410 \times 10^{-1}$	$7.268 \times 10^{-2}$	$1.030 \times 10^{-1}$	$6.504 \times 10^{-2}$	$3.214 \times 10^{-2}$	$1.453 \times 10^{-2}$
0.9700	$4.752 \times 10^{-1}$	$9.879 \times 10^{-2}$	$1.233 \times 10^{-1}$	$7.675 \times 10^{-2}$	$4.027 \times 10^{-2}$	$4.027 \times 10^{-2}$
0.9900	$5.323 \times 10^{-1}$	$1.256 \times 10^{-1}$	$1.670 \times 10^{-1}$	$1.019 \times 10^{-1}$	$6.264 \times 10^{-2}$	$3.157 \times 10^{-2}$
0.9999	$6.188 \times 10^{-1}$	$2.166 \times 10^{-1}$	$2.585 \times 10^{-1}$	$1.545 \times 10^{-1}$	$1.039 \times 10^{-1}$	$5.989 \times 10^{-2}$

Three dimensional case						
$\theta$	In-line			Staggered		
	$\lambda$	$\mathcal{K}$	$\mathcal{K}^{if}$	$\lambda$	$\mathcal{K}$	$\mathcal{K}^{if}$
0.4900	$1.093 \times 10^{-1}$	$2.769 \times 10^{-3}$	$9.280 \times 10^{-3}$	$2.333 \times 10^{-2}$	$1.421 \times 10^{-3}$	$1.507 \times 10^{-3}$
0.6300	$1.597 \times 10^{-1}$	$6.901 \times 10^{-3}$	$1.818 \times 10^{-2}$	$3.648 \times 10^{-2}$	$3.864 \times 10^{-3}$	$3.213 \times 10^{-3}$
0.7300	$2.196 \times 10^{-1}$	$1.302 \times 10^{-2}$	$3.019 \times 10^{-2}$	$5.112 \times 10^{-2}$	$7.747 \times 10^{-3}$	$5.735 \times 10^{-3}$
0.8300	$3.002 \times 10^{-1}$	$2.727 \times 10^{-2}$	$5.580 \times 10^{-2}$	$7.497 \times 10^{-2}$	$1.623 \times 10^{-2}$	$1.120 \times 10^{-2}$
0.9300	$4.098 \times 10^{-1}$	$7.172 \times 10^{-2}$	$5.580 \times 10^{-2}$	$1.267 \times 10^{-1}$	$4.209 \times 10^{-2}$	$2.876 \times 10^{-2}$
0.9500	$4.478 \times 10^{-1}$	$9.287 \times 10^{-2}$	$1.260 \times 10^{-1}$	$1.486 \times 10^{-1}$	$5.537 \times 10^{-2}$	$3.828 \times 10^{-2}$
0.9700	$5.061 \times 10^{-1}$	$1.330 \times 10^{-1}$	$1.686 \times 10^{-1}$	$1.842 \times 10^{-1}$	$7.963 \times 10^{-2}$	$5.639 \times 10^{-2}$
0.9900	$6.291 \times 10^{-1}$	$2.708 \times 10^{-1}$	$2.893 \times 10^{-1}$	$2.713 \times 10^{-1}$	$1.507 \times 10^{-1}$	$1.130 \times 10^{-1}$
0.9999	1.361	1.691	1.658	$8.687 \times 10^{-1}$	1.020	$8.966 \times 10^{-1}$

## References

- Agelinchaab, M., Tachie, M.F., Ruth, D.W., 2006. Velocity measurement of flow through a model three-dimensional porous medium. *Phys. Fluids* 18 (1), 017105.
- Airiau, C., Bottaro, A., 2020. Flow of shear-thinning fluids through porous media. *Adv. Water Resour.* 143, 103658.
- Angot, P., Bruneau, C.-H., Fabrie, P., 1999. A penalization method to take into account obstacles in incompressible viscous flows. *Numer. Math.* 81, 497–520.
- Arthur, J.K., Ruth, D.W., Tachie, M.F., 2009. PIV measurements of flow through a model porous medium with varying boundary conditions. *J. Fluid Mech.* 629, 343–374.
- Beavers, G.S., Joseph, D.D., 1967. Boundary condition at a naturally permeable wall. *J. Fluid Mech.* 30 (1), 197–207.
- Biswas, G., Breuer, M., Durst, F., 2004. Backward-facing step flows for various expansion ratios at low and moderate Reynolds numbers. *J. Fluids Eng.* 126 (3), 362–374.
- Bottaro, A., 2019. Flow over natural or engineered surfaces: an adjoint homogenization perspective. *J. Fluid Mech.* 877, P1–P91.
- Bottaro, A., Naqvi, S.B., 2020. Effective boundary conditions at a rough wall: a high-order homogenization approach. *Meccanica* 55 (9), 1781–1800.
- Bruneau, C.-H., Lasseux, D., Valdés-Parada, J.F., 2020. Comparison between direct numerical simulations and effective models for fluid-porous flows using penalization. *Meccanica* 55 (5), 1061–1077.
- Carbou, G., 2008. Brinkman model and double penalization method for the flow around a porous thin layer. *J. Math. Fluid Mech.* 10, 126–158.
- Carraro, T., Goll, C., Marciniak-Czochra, A., Mikelić, A., 2013. Pressure jump interface law for the Stokes-Darcy coupling: confirmation by direct numerical simulations. *J. Fluid Mech.* 732, 510–536.
- Chandesris, M., Jamet, D., 2006. Boundary conditions at a planar fluid porous interface for a poiseuille flow. *Int. J. Heat Mass Transf.* 49 (13), 2137–2150.
- COMSOL, Multiphysics® v. 5.4. [www.comsol.com](http://www.comsol.com). COMSOL AB, Stockholm, Sweden.
- EGGENWEILER, E., KYBAK, I., 2020. Unsuitability of the Beavers–Joseph interface condition for filtration problems. *J. Fluid Mech.* 892, A10.
- Gupte, S.K., Advani, S.G., 1997. Flow near the permeable boundary of a porous medium: an experimental investigation using LDA. *Exp. Fluids* 22 (5), 408–422.
- Jäger, W., Mikelić, A., 2001. On the roughness-induced effective boundary conditions for an incompressible viscous flow. *J. Differ. Equ.* 170, 96.
- Jamet, D., Chandresris, M., 2009. On the intrinsic nature of jump coefficients at the interface between a porous medium and a free fluid region. *Int. J. Heat Mass Transf.* 52, 289–300.
- Jones, I.P., 1973. Low Reynolds number flow past a porous spherical shell. *Proc. Camb. Philos. Soc.* 73, 231–238.
- Kuwata, Y., Suga, K., 2016. Lattice Boltzmann direct numerical simulation of interface turbulence over porous and rough walls. *Int. J. Heat Fluid Flow* 61, 145–157.
- Kuwata, Y., Suga, K., 2017. Direct numerical simulation of turbulence over anisotropic porous media. *J. Fluid Mech.* 831, 41–71.
- Lacis, U., Bagheri, S., 2016. A framework for computing effective boundary conditions at the interface between free fluid and a porous medium. *J. Fluid Mech.* 812, 866–889.
- Lacis, U., Sudhakar, Y., Pasche, S., Bagheri, S., 2020. Transfer of mass and momentum at rough and porous surfaces. *J. Fluid Mech.* 884, A21.
- Larson, R.E., Higdon, J.J.L., 1986. Microscopic flow near the surface of two-dimensional porous media. part 1. axial flow. *J. Fluid Mech.* 166, 449–472.
- Lee, C.K., Sun, C.C., Mei, C.C., 1996. Computation of permeability and dispersivities of solute or heat in periodic porous media. *Int. J. Heat Mass Transf.* 39 (4), 661–676.
- Liu, Q., Prosperetti, A., 2011. Pressure-driven flow in a channel with porous walls. *J. Fluid Mech.* 679, 77–100.
- Luminari, N., Zampogna, G., Airiau, C., Bottaro, A., 2019. A penalization method to

- treat the interface between a free-fluid region and a fibrous porous medium. *J. Porous Media* 22 (9), 1095–1107.
- Mei, C.C., Vernescu, B., 2009. *Homogenization Methods for Multiscale Mechanics*. World Sci. Pub..
- Morad, M.R., Khalili, A., 2009. Transition layer thickness in a fluid-porous medium of multi-sized spherical beads. *Exp. Fluids* 46 (2), 323–330.
- Ochoa-Tapia, J.A., Valdes-Parada, F., Goyeau, B., Lasseux, D., 2017. Fluid motion in the fluid/porous medium inter-region. *Rev. Mex. Inge. Quim.* 16 (3), 923–938.
- Ochoa-Tapia, J.A., Whitaker, S., 1995. Momentum transfer at the boundary between a porous medium and a homogeneous fluid. II. Comparison with experiment. *Int. J. Heat Mass Transf.* 38 (14), 2647–2655.
- Richardson, S., 1971. A model for the boundary condition of a porous material. Part 2. *J. Fluid Mech.* 49, 327–336.
- Saffman, P.G., 1971. On the boundary condition at the surface of a porous medium. *Stud. Appl. Math.* 50, 93–101.
- Terzis, A., Zarihos, I., Weishaupt, K., Yang, G., Chu, X., Helmig, R., Weigand, B., 2019. Microscopic velocity field measurements inside a regular porous medium adjacent to a low Reynolds number channel flow. *Phys. Fluids* 31, 042001.
- Whitaker, S., 1986. Flow in porous media. I: a theoretical derivation of Darcy's law. *Transp. Porous Media* 1 (1), 3–25.
- Zampogna, G.A., Bottaro, A., 2016. Fluid flow over and through a regular bundle of rigid fibres. *J. Fluid Mech.* 792, 5–35.
- Zampogna, G.A., Laci, U., Bagheri, S., Bottaro, A., 2019. Modeling waves in fluids flowing over and through poroelastic media. *Int. J. Multiphase Flow* 110, 148–164.